

Superconducting cavity-based sensing of band gaps in 2D materials

Krishnendu Maji,[†] Joydip Sarkar,[†] Supriya Mandal,[†] Sriram H,[†] Mahesh Hingankar,[†] Ayshi Mukherjee,[†] Soumyajit Samal,[†] Anirban Bhattacharjee,[†] Meghan P. Patankar,[†] Kenji Watanabe,[‡] Takashi Taniguchi,[¶] and Mandar M. Deshmukh^{*,†}

[†]*Department of Condensed Matter Physics and Materials Science, Tata Institute of Fundamental Research, Homi Bhabha Road, Mumbai 400005, India.*

[‡]*Research Center for Functional Materials, National Institute for Materials Science, 1-1 Namiki, Tsukuba 305-0044, Japan.*

[¶]*International Center for Materials Nanoarchitectonics, National Institute for Materials Science, 1-1 Namiki, Tsukuba 305-0044, Japan.*

E-mail: deshmukh@tifr.res.in

Abstract

The superconducting coplanar waveguide (SCPW) cavity plays an essential role in various areas like superconducting qubits, parametric amplifiers, radiation detectors, studying magnon-photon, and photon-phonon coupling. Despite its wide-ranging applications, the use of SCPW cavities to study various van der Waals 2D materials is relatively unexplored. The resonant modes of the SCPW cavity exquisitely sense the dielectric environment. In this work, we measure the charge compressibility of bilayer graphene coupled to a half-wave SCPW cavity. Our approach provides a means to

detect subtle changes in the capacitance of the bilayer graphene heterostructure, which depends on the compressibility of bilayer graphene, manifesting as shifts in the resonant frequency of the cavity. This method holds promise for exploring a wide class of van der Waals 2D materials, including transition metal dichalcogenides (TMDs) and their moiré where DC transport measurement is challenging.

Keywords: Superconducting cavity, 2D materials, bilayer graphene, microwave, capacitance

Superconducting coplanar waveguide (SCPW) cavities are structures designed to confine and manipulate electromagnetic fields at microwave frequencies,¹ which are widely used in diverse areas like coupling to superconducting qubit for readout,²⁻⁵ parametric amplifiers,^{6,7} bolometers,^{8,9} fast charge sensing of quantum dots,¹⁰ studying magnon-photon interaction in van der Waals magnets,^{11,12} studying interaction with spin ensemble,¹³⁻¹⁵ and studying nanomechanical devices.¹⁶⁻¹⁸ The SCPW cavities when operated at resonant frequency are very sensitive and find application in detecting small changes in the electromagnetic field,^{19,20} and radiation.²¹ Consequently, SCPW cavities offer powerful and sensitive tools for investigating the electronic properties of van der Waals materials.

Van der Waals 2D materials consist of atomically thin layers stacked on top of each other through weak van der Waals force. These materials exhibit extraordinary electronic, optical, and mechanical properties due to their reduced dimensionality. Furthermore, the stacking of various van der Waals materials at specific angles between layers gives rise to new functionalities and electronic properties.²²⁻²⁵ While various measurements have been conducted to study these materials, most have focused on low-frequency DC transport measurements. One of the key limitations of DC transport measurement is that it requires ohmic contact between the electrodes and 2D materials. There is a wide range of 2D materials where establishing ohmic contact is challenging. The significant advantage of the microwave technique is that it enables contactless transport measurements, such as measuring the electrical conductivity of 2D heterostructure through the transmission of

22 a capacitively coupled cavity, without the need for physical contacts or electrodes that
23 might disrupt the behavior of 2D materials. The microwave cavity-based techniques exploit
24 the extreme sensitivity of the resonant frequency to the effective dielectric or magnetic
25 environment, and the high quality factor of the cavity improves this sensitivity. Numerous
26 studies have employed microwave techniques to analyze low-dimensional materials. These
27 studies encompass diverse applications, including measuring the charge occupation of quantum
28 dots,²⁶ assessing minute capacitance,²⁷ and measuring the impedance of low-dimensional
29 materials,²⁸ exploring the microwave properties of graphene-based Josephson junction and
30 their potential applications.^{9,29–36}

31 In our work, we show an effective application of SCPW cavities to explore electronic
32 compressibility, a parameter related to the density of states (DOS) in bilayer graphene
33 (BLG). The BLG heterostructure is used as one of the coupling capacitors of a half-wave
34 ($\lambda/2$) cavity with the ability to apply gate voltages to tune its band structure.³⁷ Specifically,
35 we extract the capacitance of the BLG stack from the transmitted signal through the cavity,
36 where the resonant frequency shifts with the capacitance of the stack. This capacitance
37 measurement allows us to extract the compressibility of the BLG. Moreover, the dual gate
38 geometry of the device allows independent control of the charge density (n) in the BLG and
39 perpendicular displacement field (D). The displacement field tunes the band gap of the BLG,
40 thus modifying its DOS. Our compressibility measurement can capture this small opening of
41 the band gap. Our method could be useful in studying various other 2D materials, and bilayer
42 graphene serves as a demonstrator for the study of materials with small tunable gaps in the
43 electronic spectrum. Extending our work to other 2D heterostructures could offer a highly
44 sensitive and non-intrusive means of investigation, further enhancing our understanding of
45 various 2D materials' properties. Most of the existing techniques to measure the capacitance
46 of low-dimensional materials rely on lumped element circuits operating within a few hundred
47 kHz range.^{38,39} Whereas, our SCPW cavity operates at a few GHz frequency. The choice
48 of GHz frequency range allows scopes for fast dynamical measurements in a cavity-coupled

49 system^{10,13,40} and can be extended to 2D material platforms as well.⁴¹ A theoretical study
 50 has recently been conducted on quantum geometry-originated capacitance in insulators;⁴²
 51 measuring the capacitance of flat-band moiré systems could provide insights into the quantum
 52 geometry. In addition, the moiré platform has been proposed as a route toward the quantum
 53 simulation of correlated electronic states.⁴³ Our technique can be useful to probe many of
 54 these quantum simulators experimentally.

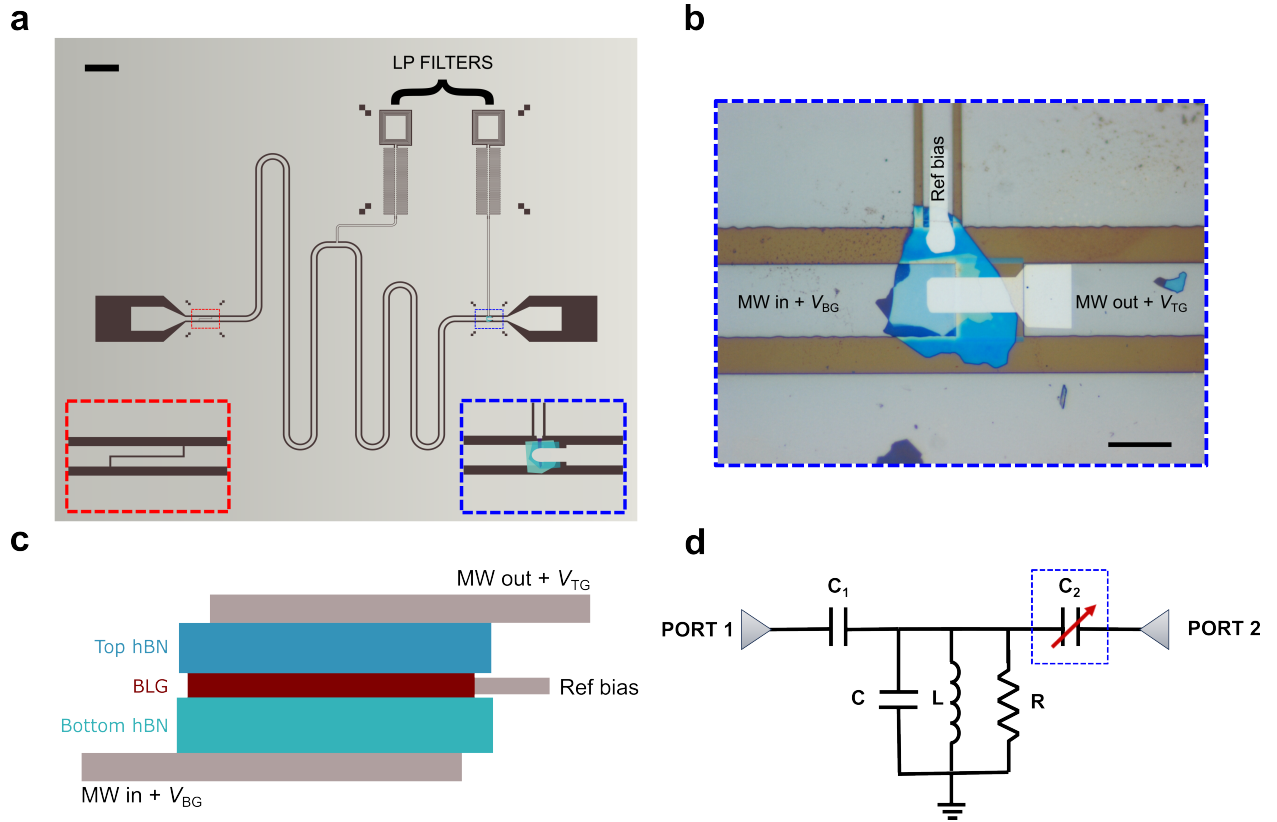


Figure 1: **Coupling the 2D heterostructure to a superconducting cavity.** **a**, The representative schematic of the device. The $\lambda/2$ cavity is designed on a MoRe-sputtered SiO_2 (280 nm)/intrinsic Si ($500 \mu\text{m}$) substrate. The inset on the bottom left shows the finger coupling capacitor designed on the left side of the cavity. The inset on the bottom right shows the zoomed-in image of the BLG heterostructure which serves as the second coupling capacitor C_2 . The scale bar on the top left is $200 \mu\text{m}$. **b**, The optical image of the BLG heterostructure. The microwave (MW) signal and applied DC voltage schemes are indicated in the figure. The scale bar is $20 \mu\text{m}$. **c**, The cross-sectional schematic of the BLG heterostructure. **d**, The schematic diagram of the equivalent circuit. The BLG stack plays the role of the coupling capacitor C_2 marked by the blue dashed box.

55 Figure 1 a shows the schematic representation of the fabricated device. The device is

56 fabricated on SiO₂ (280 nm)/intrinsic Si (500 μm) substrate. The substrate is initially
57 DC magnetron sputtered with 50 nm MoRe, a type-II superconductor. Following this,
58 photolithography and reactive ion etching are used to pattern the λ/2 SCPW cavity onto
59 the substrate. The cavity is designed to have a resonant frequency of around 6 GHz and
60 a characteristic impedance of 50 Ω. The cavity is coupled to the input and output ports
61 via coupling capacitors for transmission measurements. A finger coupling capacitor of 3.4
62 fF is designed at the input side.¹ At the output side, the van der Waals heterostructure
63 serves as the coupling capacitor. In our work, the stack consists of a BLG flake encapsulated
64 between a top hBN and a bottom hBN (see Supplementary Section 1 for details). Figure 1
65 b shows the optical image of the heterostructure. The cross-section of the heterostructure is
66 schematically shown in Figure 1 c. The bottom gate voltage is applied through a low-pass
67 (LP) filter linked to the CPW’s central conductor at the voltage node to minimize microwave
68 loss.⁴⁴ A bias tee is used to apply the top gate voltage through the output microwave port
69 (see Supplementary Section 2 for measurement details). The BLG is biased to the zero
70 potential through another LP filter. The ability to apply multi-terminal DC voltages is
71 an added advantage as many moiré heterostructures have a band structure that is widely
72 tunable with displacement field. The equivalent circuit of the device is illustrated in Figure
73 1 d, where the heterostructure plays the role of the tunable coupling capacitor C₂ which is
74 marked by the blue dashed box.

75 The measurements are done in a dilution fridge at 20 mK. The device is loaded inside
76 an aluminum puck to eliminate stray magnetic fields and create a better electromagnetic
77 environment at the base temperature. The transmission coefficient S₂₁, the ratio of the
78 transmitted signal to the input signal, is measured as a function of frequency using a vector
79 network analyzer (VNA). The amplitude and phase of the transmission coefficient, S₂₁ is
80 plotted in Figure 2 as a function of signal frequency at zero gate voltages. The π phase
81 change is the characteristic of a λ/2 cavity measured in transmission mode. The resonant
82 frequency of the cavity is around 5.152 GHz. In Supplementary Figure S2 the COMSOL

83 simulation result of the cavity is shown.

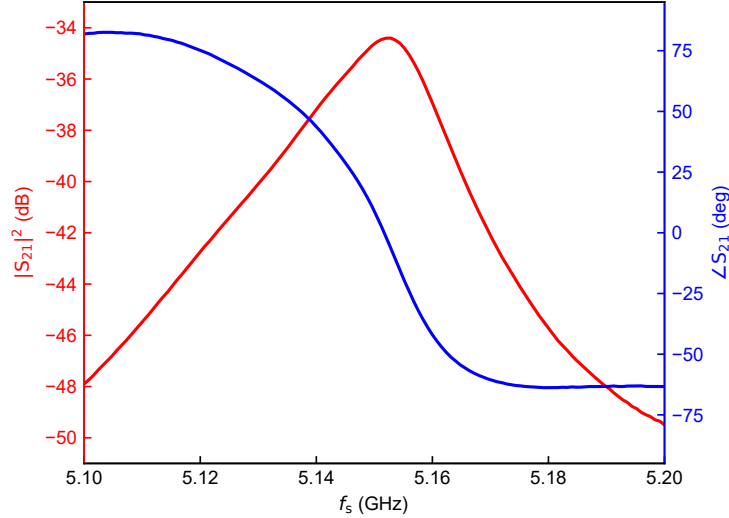


Figure 2: **Cavity characterization.** The red curve and the blue curve show the amplitude ($|S_{21}|^2$) and phase ($\angle S_{21}$) of the transmission coefficient respectively of the cavity at zero gate voltages. The resonant frequency is around 5.152 GHz. The cavity is showing a π phase change at the resonance which is the characteristic of a $\lambda/2$ cavity measured in transmission mode.

84 The device is fabricated in a dual-gate configuration, which enables independent control
 85 over the carrier density (n) of the BLG and the perpendicular displacement field (D) by
 86 adjusting both the top gate voltage (V_{TG}) and the bottom gate voltage (V_{BG}). In addition, the
 87 bilayer graphene is biased to 0 V to provide a ground reference for the DC electrostatic tuning
 88 of the system. In pristine BLG, the two graphene layers are electrically identical making it an
 89 inversion-symmetric system. Consequently, there is no band gap in its electronic structure
 90 as shown in Figure 3 b. Upon applying a perpendicular displacement field, an electrostatic
 91 potential difference is created between the two layers (shown in Figure 3 a), breaking the
 92 inversion symmetry and resulting in the opening of a band gap (shown in Figure 3 b).

93 There are two ways to probe the system experimentally. Firstly, one measures the S_{21}
 94 frequency response of the cavity-coupled device at each of the values of V_{TG} and V_{BG} creating
 95 a 4-dimensional dataset, and secondly, by observing cavity response at a frequency close to

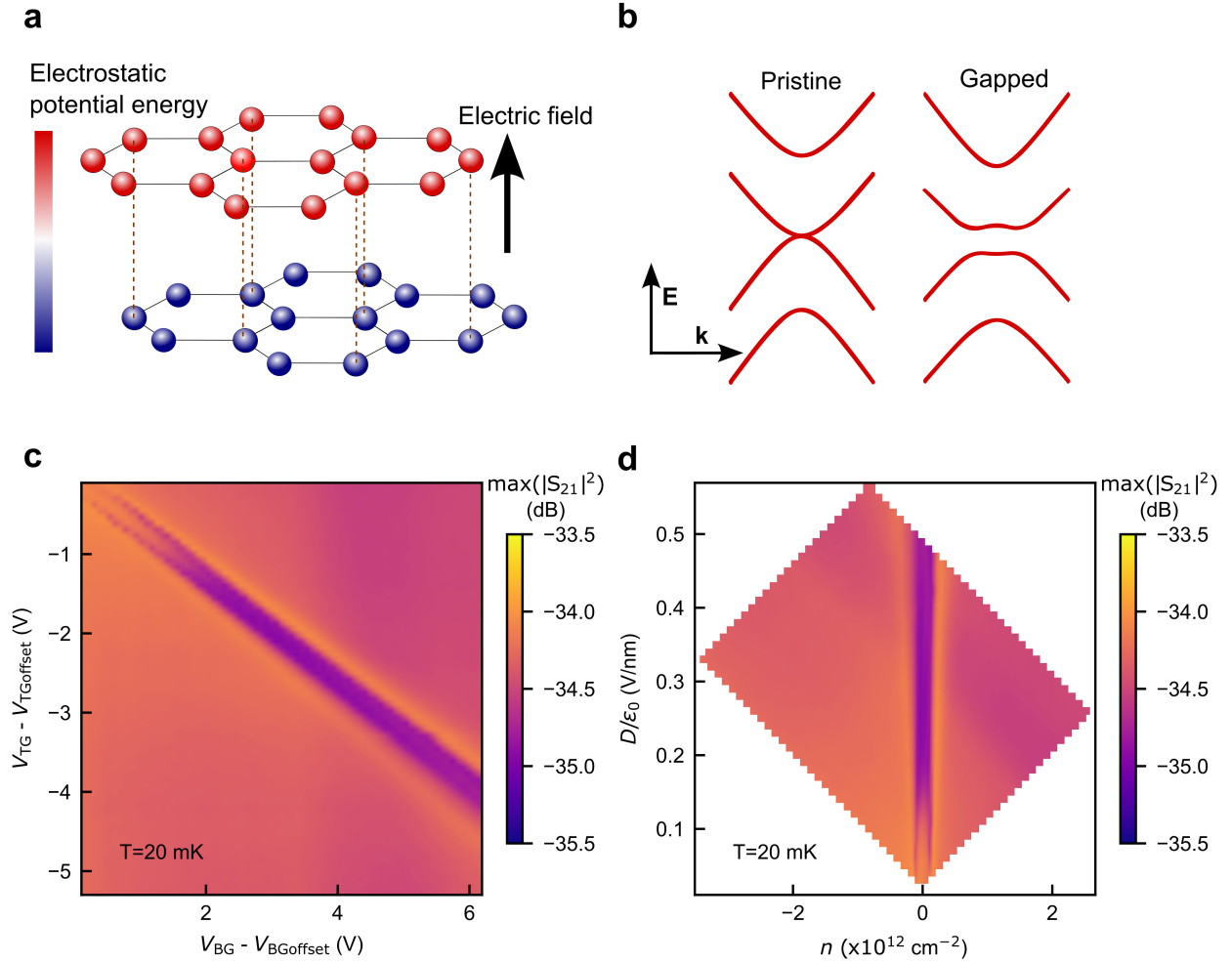


Figure 3: **The transmitted signal through the cavity as a function of the gate voltages.** **a**, Upon applying a perpendicular displacement field, an electrostatic potential energy difference is created between the two layers of bilayer graphene, resulting in the breaking of inversion symmetry. **b**, Left: The schematic shows that the pristine bilayer graphene has a zero band gap in its electronic structure. Right: Upon applying a perpendicular displacement field, a gap opens up due to the breaking of inversion symmetry. **c**, For each (V_{TG}, V_{BG}) the transmitted signal through the cavity is measured as a function of frequency. The peak value of the amplitude of the transmission coefficient, $\max(|S_{21}|^2)$ is plotted as a function of V_{BG} and V_{TG} . There is a finite offset in both V_{BG} and V_{TG} axes due to charge doping in BLG from the metallic gates. The measurements are done at 20 mK. **d**, $\max(|S_{21}|^2)$ is plotted as a function of n and D/ϵ_0 . The region of the low transmission along the displacement field corresponds to the opening of the band gap in BLG.

96 the resonant mode of the system and varying the gate voltages creating a 3-dimensional
 97 dataset. In this work, we focus on the first method of probing the system. For each $(V_{\text{TG}},$
 98 $V_{\text{BG}})$, S_{21} as a function of frequency is measured. Then the peak value of $|S_{21}|^2$ for each
 99 $(V_{\text{TG}}, V_{\text{BG}})$ is extracted from the data, which is plotted in Figure 3 c. The data is also
 100 taken on the second way where the transmission signal is measured at a fixed frequency
 101 close to the resonance (see Supplementary Figure S3). In our data, an offset of $V_{\text{BGoffset}} =$
 102 -1.15 V and $V_{\text{TGoffset}} = -2.7$ V is observed in V_{BG} and V_{TG} respectively, likely due to the
 103 charge doping in graphene from the metallic top and bottom gate which has been previously
 104 reported.⁴⁵ The data offers clearer physical insights if plotted in (n, D) space instead of $(V_{\text{BG}},$
 105 $V_{\text{TG}})$. The transformation from $(V_{\text{BG}}, V_{\text{TG}})$ to (n, D) is achieved using the following set of
 106 equations: $n = (C_{\text{BG}}V'_{\text{BG}} + C_{\text{TG}}V'_{\text{TG}})/e$ and $D = (C_{\text{BG}}V'_{\text{BG}} - C_{\text{TG}}V'_{\text{TG}})/2$, where C_{BG} (C_{TG})
 107 is the capacitance of the bottom (top) gate, $V'_{\text{BG}}(V'_{\text{TG}}) = V_{\text{BG}}(V_{\text{TG}}) - V_{\text{BGoffset}}(V_{\text{TGoffset}})$ is
 108 the offset corrected bottom (top) gate voltage, and e is the electronic charge. The plot in
 109 Figure 3 c is transformed to $(n, D/\epsilon_0)$ plane from $(V_{\text{BG}}, V_{\text{TG}})$ plane in Figure 3 d. Only
 110 the positive displacement field sector data is shown here (see Supplementary Figure S4 for
 111 the full range data). A region with low transmission appears along the electric displacement
 112 field axis. This region corresponds to the opening of a band gap in the BLG caused by the
 113 perpendicular displacement field.³⁷ The width of the low transmission region at a particular
 114 displacement field relates to the band gap of BLG at that displacement field. On looking
 115 closely at the data, one can see in the low transmission region, two subfeatures emerge.
 116 These subfeatures correspond to two charge neutrality points and can be attributed to the
 117 spatial inhomogeneous doping in the device, a consequence of its larger overall area of ~ 30
 118 μm^2 . In the data shown in Figure 3 c and d van-Hove singularity-like feature appear at the
 119 band edge of the BLG, which is a characteristic of BLG band structure (see Supplementary
 120 Section 4.3 for details).

121 To extract the capacitance of the heterostructure, the data is fitted with the scattering

122 coefficients S_{21} of a capacitively coupled $\lambda/2$ CPW cavity, which can be written as⁴⁶

$$S_{21} = \frac{2}{A + B/Z_0 + CZ_0 + D} + b, \quad (1)$$

123 where A , B , C , and D are the elements of the transmission matrix or ABCD matrix

$$124 \quad A = \cosh(\gamma l) + \frac{\sinh(\gamma l)}{j\omega C_1 Z_0}, \quad B = \sinh(\gamma l) \left(Z_0 - \frac{1}{\omega^2 C_1 C_2 Z_0} \right) + \cosh(\gamma l) \left(\frac{1}{j\omega C_1} + \frac{1}{j\omega C_2} \right)$$

$$125 \quad C = \frac{\sinh(\gamma l)}{Z_0}, \quad D = \cosh(\gamma l) + \frac{\sinh(\gamma l)}{j\omega C_2 Z_0}$$

126 where l is the length of the transmission line, $\gamma = \alpha + j\beta$ is the complex propagation constant
 127 of the microwave field, Z_0 is the characteristic impedance of the transmission line. For $\lambda/2$
 128 cavity $\beta l = \pi + \pi(\omega - \omega_0)/\omega_0$, where ω_0 is the bare resonant frequency and $\alpha l = \pi/(2Q_i)$,
 129 where Q_i is the internal quality factor of the cavity. b is to account for and adjust the
 130 reference value of the transmission signal.

131 In Figure 4 a, the resonant frequency, *i.e.* the frequency at which the amplitude of S_{21}
 132 is maximum is plotted in the $(n, D/\epsilon_0)$ plane. In Figure 4 b the frequency line-slice for
 133 two $(n, D/\epsilon_0)$ points are shown. When the BLG has an opening in the gap, its resonant
 134 frequency shifts downwards, and this frequency shift becomes more pronounced as the band
 135 gap increases.

136 For each $(n, D/\epsilon_0)$, S_{21} frequency response is fitted using Equation 1. To address
 137 the observed asymmetry in the frequency line-slice data caused by background effects, a
 138 skewness term $(1 + \text{erf}(s(f - f_0)))$ is multiplied with the fitting function, where erf is
 139 the error function and s is the skewness factor. The extracted capacitance value C_2 from
 140 the fitting is plotted in Figure 4 c (for details of the fitting procedure see Supplementary
 141 Section 5). This capacitance value, which increases when a gap opens in the BLG, directly
 142 correlates with the DOS of BLG. Using our cavity-based technique, sub-femtofarad change
 143 in capacitance can be measured accurately (see Supplementary Figure S6). The accuracy of
 144 our capacitance measurement has been compared with other state-of-the-art techniques^{38,39}
 145 (see Supplementary Section 7 for details).

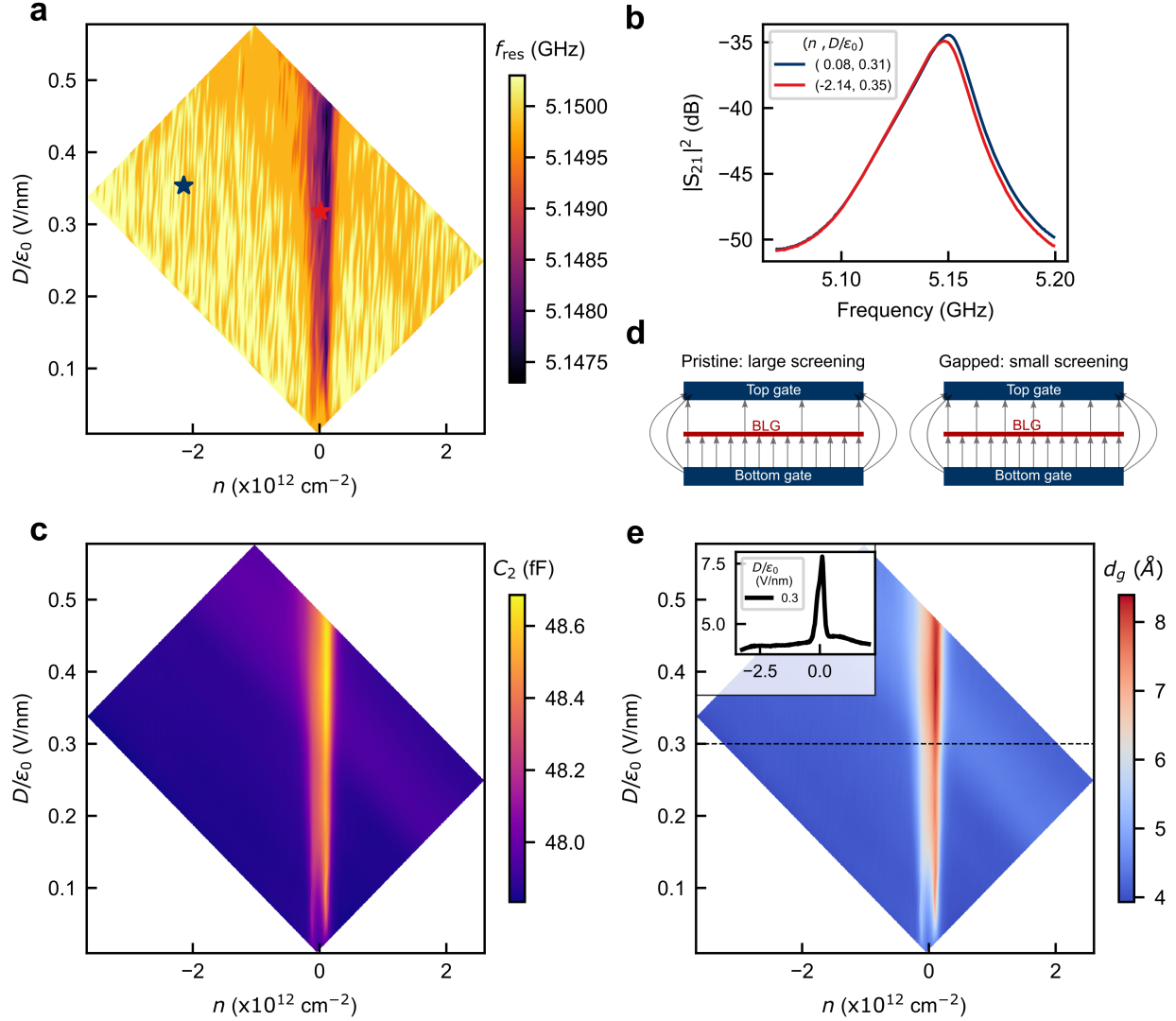


Figure 4: **Measurement of the capacitance of the BLG heterostructure.** **a**, Shows the change in resonant frequency as a function of n and D/ϵ_0 . The resonant frequency is shifting downwards with the gap opening in BLG. **b**, Shows the frequency line-slice at two $(n, D/\epsilon_0)$ points as marked in panel **a**. **c**, Shows the extracted capacitance C_2 from the fitting as a function of n and D/ϵ_0 . The capacitance increases with gap opening in BLG, which is a consequence of the decreased density of states (DOS) of the BLG, which can also be interpreted from Equation 2. **d**, Left: In pristine BLG when there is no band gap in its electronic structure, the DOS of BLG is high. The BLG acts more like a metal in this regime, thus effectively screening the electric field between the top and bottom gates. Right: With a gap opening in BLG induced by a perpendicular displacement field, the DOS of BLG significantly decreases, transforming BLG into more of an insulator. Consequently, the screening effect becomes less prominent. **e**, Shows the extracted d_g from the panel **c** using Equation 2, where d_g is related to the inverse DOS ($\frac{1}{e^2} \frac{\partial \mu}{\partial n}$) of BLG as $d_g = \frac{\epsilon_0}{e^2} \frac{\partial \mu}{\partial n}$. The inset shows the line slice of d_g with n at $D/\epsilon_0 = 0.3$ V/nm.

146 The extracted capacitance C_2 represents the penetration field capacitance between the
 147 top gate and bottom gate, where grounded BLG screens the electric field due to its finite
 148 DOS.^{39,47} By considering the BLG as an infinitely thin sheet, the expression for the measured
 149 capacitance can be written as³⁹

$$C_2 = \frac{\epsilon_0 A_t d_g \epsilon_{\text{hBN}}^2}{d_g \epsilon_{\text{hBN}} (d_b + d_t) + \epsilon_0 d_b d_t} + C_S. \quad (2)$$

150 Here A_t is the area of the top gate covering the BLG. d_b and d_t are the thickness of the
 151 bottom hBN and top hBN respectively. ϵ_{hBN} and ϵ_0 are the permittivity of hBN and free
 152 space respectively. $d_g = \frac{\epsilon_0}{e^2} \frac{\partial \mu}{\partial n}$ is the parameterization of $\frac{1}{e^2} \frac{\partial \mu}{\partial n}$ in units of length, where $\frac{\partial \mu}{\partial n}$
 153 is the inverse DOS of the BLG. The inverse DOS is related to the electronic compressibility
 154 (K) as $K^{-1} = n^2 \frac{\partial \mu}{\partial n}$. The stray capacitance C_S is assumed to be 47.81 fF, is estimated
 155 using the area of the top gate $110 \mu\text{m}^2$ and the $d_t = 32.9 \pm 0.6$ nm and $d_b = 50.1 \pm 1$
 156 nm. These thickness values have been measured using atomic force microscopy (AFM) (see
 157 Supplementary Section 6 for details). From Equation 2 one can see that the C_2 increases as
 158 the DOS decreases. In the pristine BLG, the DOS is high when there is no band gap in its
 159 electronic structure. As a result, BLG screens the electric field between the top and bottom
 160 gates more effectively resulting in a decrease in the C_2 (as depicted in Figure 4 d). Upon
 161 applying a perpendicular displacement field, a gap opens in BLG, substantially reducing the
 162 DOS. Consequently, the screening is less effective for gapped BLG (as shown in Figure 4 b),
 163 and C_2 increases.

164 From the extracted capacitance C_2 , d_g is obtained using Equation 2 and is shown in
 165 Figure 4 e. The value of d_g matches well with previous reports.³⁹ The line slice of the
 166 extracted d_g at $D/\epsilon_0=0.3$ V/nm is shown in the inset of Figure 4 e. The d_g has a sharp
 167 peak at $n = 0$ and decreases asymmetrically on either side of $n = 0$. The peak in d_g can
 168 be interpreted as the emergence of a band gap in bilayer graphene (BLG), resulting in a
 169 reduced DOS. The data can be explained by a minimal tight-binding model of BLG. The

170 inverse DOS has been calculated by solving the tight-binding Hamiltonian with a gap size
171 Δ which agrees well with the experimental data (see Supplementary Section 8 for details).⁴⁸

172 In summary, in this study, a half-wave SCPW cavity is used to characterize the electronic
173 compressibility of BLG, establishing a direct correlation between the transmitted signal
174 through the cavity and the band gap in BLG as a function of the displacement field. Also,
175 from the shift in resonant frequency, the capacitance of the stack is extracted, which directly
176 correlates with the inverse DOS of the BLG. This non-contact microwave cavity-based
177 technique provides a scope for non-invasive sensing of DOS in 2D materials.

178 Our methodology can be easily extended to the study of other 2D materials as well.
179 Furthermore, this technique holds promise for gaining insights into moiré superlattices of
180 transition metal dichalcogenides, which have gained significant attention as a promising
181 platform as a quantum simulator.⁴³ Importantly, our technique overcomes the challenge of
182 contact resistance that hampers the study of many exciting 2D materials. In addition, the
183 choice of microwave frequencies will also enable fast dynamical measurements^{10,13,40} in a
184 cavity-coupled 2D van der Waals system.

185 The Supporting Information is available free of charge via the internet at <http://pubs.acs.org>.
186 The Supporting Information contains device fabrication, measurement details, COMSOL
187 simulation, additional data, fitting procedure, atomic force microscopy of the hBN flakes,
188 comparison with other works, and density of states calculation of bilayer graphene.

189 **Acknowledgement**

190 We thank R. Vijay and V. Singh for their helpful discussions and comments. We thank
191 H. Agarwal, and D. Jangade for helping with device fabrication, and S. Layek for helping
192 with data analysis. We thank U. Ghorai for helping with the tight binding calculation. We
193 acknowledge Nanomission grant SR/NM/NS-45/2016 and the DST SUPRA SPR/2019/001247
194 grant, along with the Department of Atomic Energy of Government of India (12-R&D-TFR-5.10-0100)

195 for support. We also acknowledge support from the Department of Science and Technology,
196 India, via the QuEST programme. MMD acknowledges support from J.C. Bose Fellowship
197 JCB/2022/000045 from the Department of Science and Technology of India. Preparation
198 of hBN single crystals were supported by the Elemental Strategy Initiative conducted by
199 the Ministry of Education, Culture, Sports, Science and Technology, Japan (grant number
200 JPMXP0112101001) and Japan Society for the Promotion of Science KAKENHI (grant
201 numbers 19H05790 and JP20H00354).

202 **References**

- 203 (1) Göppl, M.; Fragner, A.; Baur, M.; Bianchetti, R.; Filipp, S.; Fink, J. M.; Leek, P. J.;
204 Puebla, G.; Steffen, L.; Wallraff, A. Coplanar waveguide resonators for circuit quantum
205 electrodynamics. *Journal of Applied Physics* **2008**, *104*, 113904.
- 206 (2) Wallraff, A.; Schuster, D. I.; Blais, A.; Frunzio, L.; Huang, R.-S.; Majer, J.; Kumar, S.;
207 Girvin, S. M.; Schoelkopf, R. J. Strong coupling of a single photon to a superconducting
208 qubit using circuit quantum electrodynamics. *Nature* **2004**, *431*, 162–167, Number:
209 7005 Publisher: Nature Publishing Group.
- 210 (3) Wallraff, A.; Schuster, D. I.; Blais, A.; Frunzio, L.; Majer, J.; Devoret, M. H.;
211 Girvin, S. M.; Schoelkopf, R. J. Approaching Unit Visibility for Control of a
212 Superconducting Qubit with Dispersive Readout. *Physical Review Letters* **2005**, *95*,
213 060501.
- 214 (4) Schuster, D. I.; Houck, A. A.; Schreier, J. A.; Wallraff, A.; Gambetta, J. M.; Blais, A.;
215 Frunzio, L.; Majer, J.; Johnson, B.; Devoret, M. H.; Girvin, S. M.; Schoelkopf, R. J.
216 Resolving photon number states in a superconducting circuit. *Nature* **2007**, *445*,
217 515–518, Number: 7127 Publisher: Nature Publishing Group.
- 218 (5) Majer, J.; Chow, J. M.; Gambetta, J. M.; Koch, J.; Johnson, B. R.; Schreier, J. A.;

- 219 Frunzio, L.; Schuster, D. I.; Houck, A. A.; Wallraff, A.; Blais, A.; Devoret, M. H.;
220 Girvin, S. M.; Schoelkopf, R. J. Coupling superconducting qubits via a cavity bus.
221 *Nature* **2007**, *449*, 443–447, Number: 7161 Publisher: Nature Publishing Group.
- 222 (6) Tholén, E. A.; Ergül, A.; Doherty, E. M.; Weber, F. M.; Grégis, F.; Haviland, D. B.
223 Nonlinearities and parametric amplification in superconducting coplanar waveguide
224 resonators. *Applied Physics Letters* **2007**, *90*, 253509.
- 225 (7) Castellanos-Beltran, M. A.; Lehnert, K. W. Widely tunable parametric amplifier based
226 on a superconducting quantum interference device array resonator. *Applied Physics*
227 *Letters* **2007**, *91*, 083509.
- 228 (8) Day, P. K.; LeDuc, H. G.; Mazin, B. A.; Vayonakis, A.; Zmuidzinas, J. A broadband
229 superconducting detector suitable for use in large arrays. *Nature* **2003**, *425*, 817–821,
230 Number: 6960 Publisher: Nature Publishing Group.
- 231 (9) Lee, G.-H.; Efetov, D. K.; Jung, W.; Ranzani, L.; Walsh, E. D.; Ohki, T. A.;
232 Taniguchi, T.; Watanabe, K.; Kim, P.; Englund, D.; Fong, K. C. Graphene-based
233 Josephson junction microwave bolometer. *Nature* **2020**, *586*, 42–46, Number: 7827
234 Publisher: Nature Publishing Group.
- 235 (10) Stehlik, J.; Liu, Y.-Y.; Quintana, C.; Eichler, C.; Hartke, T.; Petta, J. Fast Charge
236 Sensing of a Cavity-Coupled Double Quantum Dot Using a Josephson Parametric
237 Amplifier. *Physical Review Applied* **2015**, *4*, 014018, Publisher: American Physical
238 Society.
- 239 (11) Hou, J. T.; Liu, L. Strong Coupling between Microwave Photons and Nanomagnet
240 Magnons. *Physical Review Letters* **2019**, *123*, 107702.
- 241 (12) Mandal, S.; Kapoor, L. N.; Ghosh, S.; Jesudasan, J.; Manni, S.; Thamizhavel, A.;
242 Raychaudhuri, P.; Singh, V.; Deshmukh, M. M. Coplanar cavity for strong coupling

- 243 between photons and magnons in van der Waals antiferromagnet. *Applied Physics*
244 *Letters* **2020**, *117*, 263101.
- 245 (13) Amsüss, R.; Koller, C.; Nöbauer, T.; Putz, S.; Rotter, S.; Sandner, K.; Schneider, S.;
246 Schramböck, M.; Steinhauser, G.; Ritsch, H.; Schmiedmayer, J.; Majer, J. Cavity QED
247 with Magnetically Coupled Collective Spin States. *Physical Review Letters* **2011**, *107*,
248 060502, Publisher: American Physical Society.
- 249 (14) Kubo, Y.; Ong, F. R.; Bertet, P.; Vion, D.; Jacques, V.; Zheng, D.; Dréau, A.;
250 Roch, J.-F.; Auffeves, A.; Jelezko, F.; Wrachtrup, J.; Barthe, M. F.; Bergonzo, P.;
251 Esteve, D. Strong Coupling of a Spin Ensemble to a Superconducting Resonator.
252 *Physical Review Letters* **2010**, *105*, 140502, Publisher: American Physical Society.
- 253 (15) Ranjan, V.; de Lange, G.; Schutjens, R.; Debelhoir, T.; Groen, J. P.; Szombati, D.;
254 Thoen, D. J.; Klapwijk, T. M.; Hanson, R.; DiCarlo, L. Probing Dynamics of an
255 Electron-Spin Ensemble via a Superconducting Resonator. *Physical Review Letters*
256 **2013**, *110*, 067004, Publisher: American Physical Society.
- 257 (16) Regal, C. A.; Teufel, J. D.; Lehnert, K. W. Measuring nanomechanical motion with
258 a microwave cavity interferometer. *Nature Physics* **2008**, *4*, 555–560, Number: 7
259 Publisher: Nature Publishing Group.
- 260 (17) Singh, V.; Bosman, S. J.; Schneider, B. H.; Blanter, Y. M.; Castellanos-Gomez, A.;
261 Steele, G. A. Optomechanical coupling between a multilayer graphene mechanical
262 resonator and a superconducting microwave cavity. *Nature Nanotechnology* **2014**, *9*,
263 820–824, Number: 10 Publisher: Nature Publishing Group.
- 264 (18) Sahu, S. K.; Mandal, S.; Ghosh, S.; Deshmukh, M. M.; Singh, V. Superconducting
265 Vortex-Charge Measurement Using Cavity Electromechanics. *Nano Letters* **2022**, *22*,
266 1665–1671, Publisher: American Chemical Society.

- 267 (19) Schmidt, F. E.; Bothner, D.; Rodrigues, I. C.; Gely, M. F.; Jenkins, M. D.; Steele, G. A.
268 Current Detection Using a Josephson Parametric Upconverter. *Physical Review Applied*
269 **2020**, *14*, 024069, Publisher: American Physical Society.
- 270 (20) Endo, Y.; Onishi, M.; Muroga, S.; Arai, K.; Yanagi, K.; Shimada, Y.; Yamaguchi, M.
271 GHz Range Magnetic Field Measurement of a Coplanar Waveguide with a Magnetic
272 Force Microscope Tip by Exploiting a Beat Signal Between the Coplanar Waveguide
273 and an Exciting Coil. *IEEE Transactions on Magnetics* **2014**, *50*, 1–4, Conference
274 Name: IEEE Transactions on Magnetics.
- 275 (21) de Visser, P. J.; Baselmans, J. J. A.; Bueno, J.; Llombart, N.; Klapwijk, T. M.
276 Fluctuations in the electron system of a superconductor exposed to a photon flux.
277 *Nature Communications* **2014**, *5*, 3130, Number: 1 Publisher: Nature Publishing
278 Group.
- 279 (22) Cao, Y.; Fatemi, V.; Demir, A.; Fang, S.; Tomarken, S. L.; Luo, J. Y.;
280 Sanchez-Yamagishi, J. D.; Watanabe, K.; Taniguchi, T.; Kaxiras, E.; Ashoori, R. C.;
281 Jarillo-Herrero, P. Correlated insulator behaviour at half-filling in magic-angle graphene
282 superlattices. *Nature* **2018**, *556*, 80–84, Number: 7699 Publisher: Nature Publishing
283 Group.
- 284 (23) Cao, Y.; Fatemi, V.; Fang, S.; Watanabe, K.; Taniguchi, T.; Kaxiras, E.;
285 Jarillo-Herrero, P. Unconventional superconductivity in magic-angle graphene
286 superlattices. *Nature* **2018**, *556*, 43–50, Number: 7699 Publisher: Nature Publishing
287 Group.
- 288 (24) Ma, C.; Wang, Q.; Mills, S.; Chen, X.; Deng, B.; Yuan, S.; Li, C.; Watanabe, K.;
289 Taniguchi, T.; Du, X.; Zhang, F.; Xia, F. Moiré Band Topology in Twisted Bilayer
290 Graphene. *Nano Letters* **2020**, *20*, 6076–6083, Publisher: American Chemical Society.
- 291 (25) Pan, Y.; Fölsch, S.; Nie, Y.; Waters, D.; Lin, Y.-C.; Jariwala, B.; Zhang, K.; Cho, K.;

- 292 Robinson, J. A.; Feenstra, R. M. Quantum-Confined Electronic States Arising from
293 the Moiré Pattern of MoS₂–WSe₂ Heterobilayers. *Nano Letters* **2018**, *18*, 1849–1855,
294 Publisher: American Chemical Society.
- 295 (26) Schoelkopf, R. J.; Wahlgren, P.; Kozhevnikov, A. A.; Delsing, P.; Prober, D. E.
296 The Radio-Frequency Single-Electron Transistor (RF-SET): A Fast and Ultrasensitive
297 Electrometer. *Science* **1998**, *280*, 1238–1242, Publisher: American Association for the
298 Advancement of Science.
- 299 (27) Malinowski, F. K.; Han, L.; De Jong, D.; Wang, J.-Y.; Prosko, C. G.; Badawy, G.;
300 Gazibegovic, S.; Liu, Y.; Krogstrup, P.; Bakkers, E. P.; Kouwenhoven, L. P.; Koski, J. V.
301 Radio-Frequency C - V Measurements with Subattofarad Sensitivity. *Physical Review*
302 *Applied* **2022**, *18*, 024032.
- 303 (28) Johmen, T.; Shinozaki, M.; Fujiwara, Y.; Aizawa, T.; Otsuka, T. Radio-Frequency
304 Reflectometry in Bilayer Graphene Devices Utilizing Microscale Graphite Back-Gates.
305 *Physical Review Applied* **2023**, *20*, 014035.
- 306 (29) Schmidt, F. E.; Jenkins, M. D.; Watanabe, K.; Taniguchi, T.; Steele, G. A. A ballistic
307 graphene superconducting microwave circuit. *Nature Communications* **2018**, *9*, 4069,
308 Number: 1 Publisher: Nature Publishing Group.
- 309 (30) Dou, Z.; Wakamura, T.; Virtanen, P.; Wu, N.-J.; Deblock, R.; Autier-Laurent, S.;
310 Watanabe, K.; Taniguchi, T.; Guéron, S.; Bouchiat, H.; Ferrier, M. Microwave
311 photoassisted dissipation and supercurrent of a phase-biased graphene-superconductor
312 ring. *Physical Review Research* **2021**, *3*, L032009, Publisher: American Physical
313 Society.
- 314 (31) Haller, R.; Fülöp, G.; Indolese, D.; Ridderbos, J.; Kraft, R.; Cheung, L. Y.;
315 Ungerer, J. H.; Watanabe, K.; Taniguchi, T.; Beckmann, D.; Danneau, R.; Virtanen, P.;
316 Schönenberger, C. Phase-dependent microwave response of a graphene Josephson

- 317 junction. *Physical Review Research* **2022**, *4*, 013198, Publisher: American Physical
318 Society.
- 319 (32) Kroll, J. G.; Uilhoorn, W.; van der Enden, K. L.; de Jong, D.; Watanabe, K.;
320 Taniguchi, T.; Goswami, S.; Cassidy, M. C.; Kouwenhoven, L. P. Magnetic field
321 compatible circuit quantum electrodynamics with graphene Josephson junctions.
322 *Nature Communications* **2018**, *9*, 4615, Number: 1 Publisher: Nature Publishing
323 Group.
- 324 (33) Kokkonen, R.; Girard, J.-P.; Hazra, D.; Laitinen, A.; Govenius, J.; Lake, R. E.;
325 Sallinen, I.; Vesterinen, V.; Partanen, M.; Tan, J. Y.; Chan, K. W.; Tan, K. Y.;
326 Hakonen, P.; Möttönen, M. Bolometer operating at the threshold for circuit quantum
327 electrodynamics. *Nature* **2020**, *586*, 47–51, Number: 7827 Publisher: Nature
328 Publishing Group.
- 329 (34) Sarkar, J.; Salunkhe, K. V.; Mandal, S.; Ghatak, S.; Marchawala, A. H.; Das, I.;
330 Watanabe, K.; Taniguchi, T.; Vijay, R.; Deshmukh, M. M. Quantum-noise-limited
331 microwave amplification using a graphene Josephson junction. *Nature Nanotechnology*
332 **2022**, *17*, 1147–1152, Number: 11 Publisher: Nature Publishing Group.
- 333 (35) Butseraen, G.; Ranadive, A.; Aparicio, N.; Rafsanjani Amin, K.; Juyal, A.;
334 Esposito, M.; Watanabe, K.; Taniguchi, T.; Roch, N.; Lefloch, F.; Renard, J. A
335 gate-tunable graphene Josephson parametric amplifier. *Nature Nanotechnology* **2022**,
336 *17*, 1153–1158, Number: 11 Publisher: Nature Publishing Group.
- 337 (36) Wang, J. I.-J. et al. Coherent control of a hybrid superconducting circuit made with
338 graphene-based van der Waals heterostructures. *Nature Nanotechnology* **2019**, *14*,
339 120–125, Number: 2 Publisher: Nature Publishing Group.
- 340 (37) Zhang, Y.; Tang, T.-T.; Girit, C.; Hao, Z.; Martin, M. C.; Zettl, A.; Crommie, M. F.;
341 Shen, Y. R.; Wang, F. Direct observation of a widely tunable bandgap in bilayer

- 342 graphene. *Nature* **2009**, *459*, 820–823, Number: 7248 Publisher: Nature Publishing
343 Group.
- 344 (38) Young, A. F.; Dean, C. R.; Meric, I.; Sorgenfrei, S.; Ren, H.; Watanabe, K.;
345 Taniguchi, T.; Hone, J.; Shepard, K. L.; Kim, P. Electronic compressibility of
346 layer-polarized bilayer graphene. *Physical Review B* **2012**, *85*, 235458.
- 347 (39) Henriksen, E. A.; Eisenstein, J. P. Measurement of the electronic compressibility of
348 bilayer graphene. *Physical Review B* **2010**, *82*, 041412.
- 349 (40) Pirkkalainen, J.-M.; Cho, S. U.; Li, J.; Paraoanu, G. S.; Hakonen, P. J.; Sillanpää, M. A.
350 Hybrid circuit cavity quantum electrodynamics with a micromechanical resonator.
351 *Nature* **2013**, *494*, 211–215, Number: 7436 Publisher: Nature Publishing Group.
- 352 (41) Yoo, H. M.; Korkusinski, M.; Miravet, D.; Baldwin, K. W.; West, K.; Pfeiffer, L.;
353 Hawrylak, P.; Ashoori, R. C. Time, momentum, and energy resolved pump-probe
354 tunneling spectroscopy of two-dimensional electron systems. *Nature Communications*
355 **2023**, *14*, 7440, Number: 1 Publisher: Nature Publishing Group.
- 356 (42) Komissarov, I.; Holder, T.; Queiroz, R. The quantum geometric origin of capacitance
357 in insulators. *arXiv:2306.08035 [cond-mat]* , 2023, <http://arxiv.org/abs/2306.08035>.
- 358 (43) Kennes, D. M.; Claassen, M.; Xian, L.; Georges, A.; Millis, A. J.; Hone, J.;
359 Dean, C. R.; Basov, D. N.; Pasupathy, A. N.; Rubio, A. Moiré heterostructures as
360 a condensed-matter quantum simulator. *Nature Physics* **2021**, *17*, 155–163.
- 361 (44) Mi, X.; Cady, J. V.; Zajac, D. M.; Stehlik, J.; Edge, L. F.; Petta, J. R. Circuit quantum
362 electrodynamics architecture for gate-defined quantum dots in silicon. *Applied Physics*
363 *Letters* **2017**, *110*, 043502.
- 364 (45) Nouchi, R.; Saito, T.; Tanigaki, K. Determination of Carrier Type Doped from Metal

- 365 Contacts to Graphene by Channel-Length-Dependent Shift of Charge Neutrality Points.
366 *Applied Physics Express* **2011**, *4*, 035101, Publisher: IOP Publishing.
- 367 (46) Chen, Q.-M.; Pfeiffer, M.; Partanen, M.; Fesquet, F.; Honasoge, K. E.; Kronowetter, F.;
368 Nojiri, Y.; Renger, M.; Fedorov, K. G.; Marx, A.; Deppe, F.; Gross, R. Scattering
369 coefficients of superconducting microwave resonators. I. Transfer matrix approach.
370 *Physical Review B* **2022**, *106*, 214505, Publisher: American Physical Society.
- 371 (47) Young, A. F.; Levitov, L. S. Capacitance of graphene bilayer as a probe of layer-specific
372 properties. *Physical Review B* **2011**, *84*, 085441.
- 373 (48) McCann, E.; Koshino, M. The electronic properties of bilayer graphene. *Reports on*
374 *Progress in Physics* **2013**, *76*, 056503, Publisher: IOP Publishing.